Effect of Fuel Cetane Number on the Performance of Catalyst-Heating Operation in a Medium-duty Diesel Engine

Author, co-author (Do NOT enter this information. It will be pulled from participant tab in MyTechZone)

Affiliation (Do NOT enter this information. It will be pulled from participant tab in MyTechZone)

Abstract

To comply with increasingly stringent pollutant emissions regulations, diesel engine operation in a catalyst-heating mode is critical to achieve rapid light-off of exhaust aftertreatment catalysts during the first minutes of cold starting. Current approaches to catalyst-heating operation typically involve one or more late post injections to retard combustion phasing and increase exhaust temperatures. The ability to retard post injection timing(s) while maintaining acceptable pollutant emissions levels is pivotal for improved catalyst-heating calibrations. Higher fuel cetane number has been reported to enable later post injections with increased exhaust heat and decreased pollutant emissions, but the mechanism is not well understood. The purpose of this experimental and numerical simulation study is to provide further insight into the ways in which fuel cetane number affects combustion and pollutant formation in a medium-duty diesel engine.

Three full boiling-range diesel fuels with cetane numbers of approximately 45, 50, and 55 are employed in this study with a well-controlled set of calibrations employing a five-injection strategy. The two post injections are block-shifted to increasingly retarded timings, and the effects on exhaust heat and pollutant emissions are quantified for each fuel. For a given injection strategy calibration, increasing cetane number enables increased exhaust temperature and decreased hydrocarbon and carbon monoxide emissions for a fixed load. The increase in exhaust temperature is attributed to an increased fueling requirement to compensate for additional wall heat losses caused by earlier, more robust pilot combustion with the more reactive fuels. Formaldehyde is predicted to form in the fuel-lean periphery of the first pilot injection spray and can persist until exhaust valve opening in the absence of direct interactions with subsequent injections. Unreacted fuel-air mixture in the fuel-rich interior of the first-pilot spray is likely too cool for any significant reactions, and can persist until exhaust valve opening in the absence of turbulence/chemistry interactions and/or direct heating through interactions with subsequent injections.

Introduction

Catalyst-heating operation during the first minutes of diesel engine start-up is used to rapidly increase the diesel oxidation and selective catalytic reduction (SCR) catalysts' temperatures and to quickly reach their light off temperatures [2]. Before the activation of the catalysts, the pollutant emissions produced in the combustion chamber are emitted to the tailpipe. To cope with upcoming stringent nitrogen oxide emissions regulations, it is essential to develop effective catalyst-heating operation strategies.

For a given configuration of an engine and its accessories, the mass flow rate and temperature of the engine exhaust are the most critical factors for delivering enthalpy to the catalysts to promote light-off. In diesel engines, fuel injection parameters are the most significant control factors for varying the exhaust energy flow. Flexible and precise control of the fuel delivery has been enabled by common-rail fuel injection systems and injector technologies which enables use of complex multiple-injection strategies in catalyst-heating operation [3].

Although conventional diesel fuel is more reactive than other transportation fuels such as gasoline, the in-cylinder conditions under catalyst-heating operation are very unfriendly (low pressure and temperature) toward successful combustion. In addition, the calibration process is very difficult due to tradeoffs between increasing exhaust enthalpy, thermodynamic efficiency, and emissions. The reactivity of the fuel can also play a significant role in these complex tradeoffs.

It was previously reported that increased fuel cetane number (CN) enables hotter and cleaner catalyst-heating operation [3] with an optimized engine calibration. A remarkable finding was that increased CN enabled higher exhaust temperatures and enthalpy flows with simultaneous reductions of criteria pollutant emissions. However, this applied research did not provide a sufficient fundamental understanding of the mechanisms by which CN enables such improvements.

Previous investigations of catalyst-heating operation in a single-cylinder, medium-duty diesel research engine provided insight into the tradeoffs between thermodynamic performance and pollutant emissions [1]. A space-filling statistical experimental design was used to study a large calibration-parameter space. However, despite varying fuel reactivity with a cetane improver, the experiments did not clarify the mechanisms by which more reactive fuels may enable improved catalyst-heating calibrations, as increased fuel reactivity was frequently observed to decrease exhaust temperatures for a fixed calibration.

This study is a continuation of the previous work [1] to clarify the mechanisms by which fuel CN affects engine performance during catalyst-heating operation. The exhaust gas recirculation (EGR) rate

10/19/2016

and injection strategy calibration that produced the highest exhaust heat flux in the previous study is chosen as the baseline for this study. A post injection retardability test is developed by block-shifting two post injections to more retarded timings while measuring their effects on exhaust temperature and pollutant emissions. The retardability test is repeated with three different post injection energizing time ratios, and with fuels having three different CNs. Detailed thermodynamic analyses are combined with a one-dimensional spray model and chemical kinetic simulations to provide further insight into some of the mechanisms by which CN affects exhaust temperature and unburned hydrocarbon emissions.

Methodology

Engine and catalyst heating operation

The engine used in this study is a single-cylinder, medium-duty diesel research engine based on the Ford 6.7 L eight-cylinder engine. The connecting rod, piston, and 8-hole fuel injector are all production parts. Table 1 provides additional geometric information of the engine. The experimental system used in this study is well described in the previous investigation [1], so detailed descriptions are avoided for brevity's sake. The engine and its auxiliary systems are depicted in Figure 1.

Table 1: Engine hardware features. The compression ratio is computed for this operating point using thermodynamic techniques (see, for example, [1, 4])

Bore	99 mm
Stroke	108 mm

Displacement volume	0.8315 L
Compression ratio	16.5:1
Valves	4
Fuel injector	8-hole piezo

The operating conditions are chosen to represent catalyst-heating operation during the cold-start phase, as summarized in Table 2. In reality, the engine is at the ambient temperature before start-up, and during catalyst-heating operation there is a significant transient in engine, oil, and coolant temperatures. This effect is neglected for the single-cylinder engine experiment in this study. Instead, the coolant and intake temperatures are chosen as the lowest temperature that can be achieved in the laboratory. Due to undersized cooling units, the coolant temperatures during the experiment slightly increase over time, but are maintained within 35–40°C for all operating conditions. Oil temperature also varied between 39 to 42°C throughout the experimental campaign. However, the experimental protocol is strictly held consistent for all different fuels. As a result, the discrepancies in coolant and oil temperatures are less than 0.5°C for a case-to-case comparison.

Intake temperature is strictly held constant at 35°C throughout the experimental campaign. The load is maintained at 3.25 bar of net indicated mean effective pressure ($IMEP_n$) by adjusting the main injection quantity as post injection timings and/or fuel is changed. The intake mass flow rate and composition are also held constant to simulate a 5% EGR rate. Nitrogen (N_2) and carbon dioxide (CO_2) are used together with excess air to match the heat capacity and density that would result from the use of actual EGR.
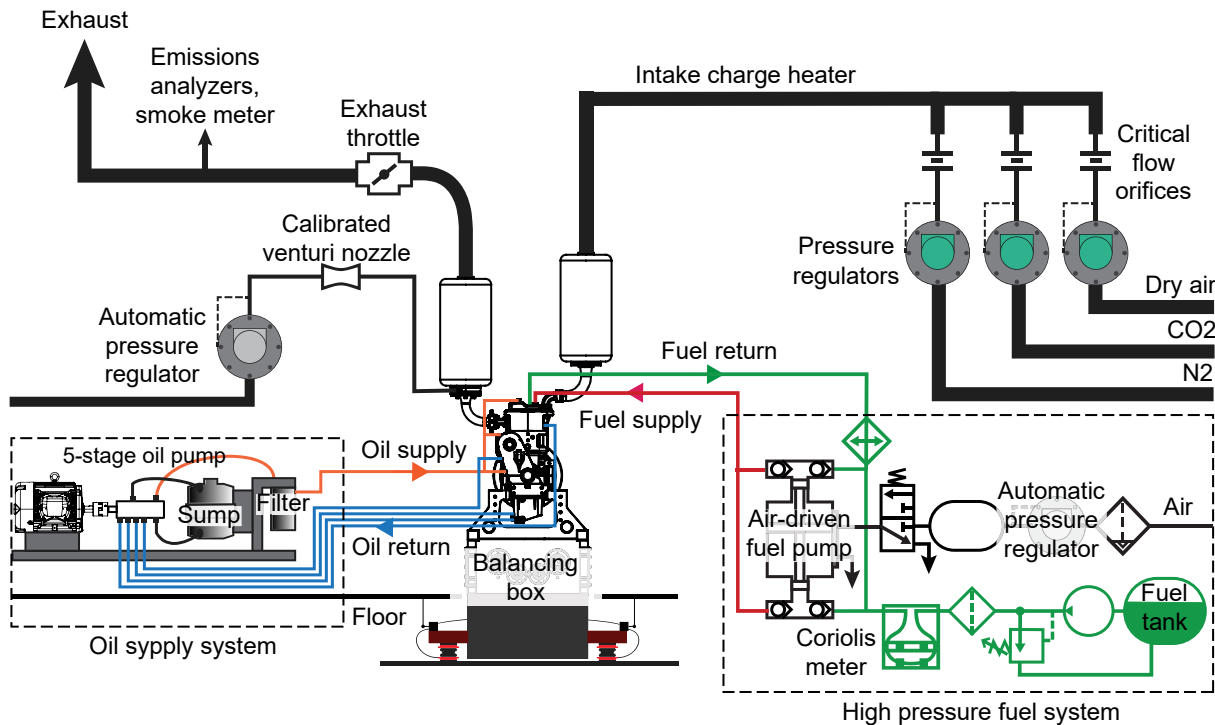

Figure 1: Simplified sketch of the medium-duty diesel combustion research lab at Sandia National Laboratories [1]. Items are not drawn to scale and the coolant conditioning system is not shown.

10/19/2016

Table 2: Engine operating conditions

Coolant temperature	35 °C– 40 °C*
Oil temperature	39 °C – 42 °C*
Intake temperature	35 °C ± 0.3 °C
Engine speed	1200 rev min^{-1}
IMEP$_n$	3.25 bar ± 0.1 bar
Intake flow rate	7.5 g/s
Intake pressure (not controlled)	92.4 kPa – 92.9 kPa
Simulated EGR rate	5 %
Intake [O$_2$]	20.557 %
Intake [CO$_2$]	0.379 %
Exhaust back pressure	128 kPa ± 0.3 kPa
Exhaust dilution flow rate	10 g/s
Rail pressure	700 bar ± 3 bar
Injection strategy	2 pilots, 1 main, 2 posts

* within 0.5 °C for case-to-case comparison

The injection strategy calibration that provided the hottest exhaust temperature at the 5% EGR level in the authors' previous study [1] is taken as the baseline for this study. The injection parameters used in this study are shown in Table 3. The two post injections are retarded from their baseline timing by block-shifting. The energizing-time of the second post injection is varied from 351 μs (baseline, injection strategy A) to 299 μs (B) and 198 μs (C), while maintaining the total sum of post injections durations at 599 μs. Approximate numbers of injection masses are provided from measurement (Moehwald HDA) at baseline condition. The main injection amount at the baseline is approximately 6.2 mg/cycle. The conceptual depiction of the injection strategies is shown in Figure 2 to visualize how the two post injections are changed.

Table 3: Injection parameters

| Start of energizing (SOE) of 1st pilot (fixed)	-18.25 CA aTDC
1st pilot mass (approximate, continuous)	2.16 mg/cycle*
Dwell between 1st and 2nd pilot (fixed)	1102 μs
2nd pilot mass (approximate, continuous)	2.05 mg/cycle*
Dwell between 2nd pilot and main (fixed)	1151 μs
Duration of energizing (DOE) of main; continuous variable	Varied to maintain load
Dwell between main and 1st post; discrete variable	[2695:400:4695] μs (6 variations)
DOE of 1st post + 2nd post (fixed)	599 μs
Total post mass (approximate, continuous)	10.73 mg/cycle*
DOE of 1st post; discrete variable	(A) 248, (B) 300, (C) 401 μs
DOE of 2nd post; discrete variable	(A) 351, (B) 299, (C) 198 μs

* at baseline condition
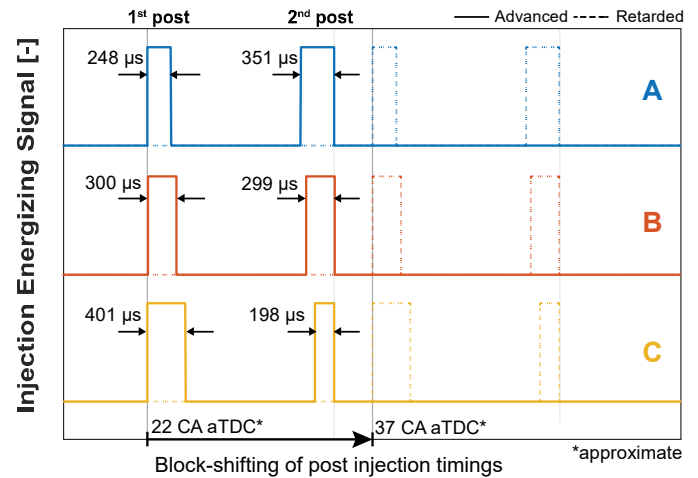
Figure 2: Energizing schedules for post injections utilized in this work. The solid lines represent the most advanced, baseline timings, and the dashed lines represent the most retarded timings. Starting crank angles for each post injection is approximate as the main injection duration varies.

Fuels

A portion of this work has been funded by the U.S. Department of Energy's Co-Optimization of Fuels and Engines program [5]. Within this program, a set of well-controlled fuels with varying distillation curves and three different CNs have been procured. The fuels with varying CNs are used in this study, and their properties are summarized in Table 4. While the fuels are referred to as CN45, CN50, and CN55, the measured CN values are 45.3, 49.9, and 54.3, respectively. Most of the fuel properties are very similar, but energy density slightly increases as CN increases.

Fuel	CN45	CN50	CN55
Cetane rating	45.3	49.9	54.3
Aromatic content	14.4 vol%	14.3 vol%	14.9 vol%
Olefin content	0.6 vol%	0.6 vol%	0.4 vol%
Saturate content	85.0 vol%	85.1 vol%	84.7 vol%
H/C ratio	1.892	1.897	1.897
O/C ratio	0	0	0
Density @ 15°C	816.2 kg/m³	812.4 kg/m³	808.3 kg/m³
Lower heating value	43.23 MJ/kg	43.28 MJ/kg	43.31 MJ/kg
Distillation temperature, IBP	186.9°C	187.1°C	189.3°C
Distillation temperature, 10%	197.5°C	202.6°C	205.9°C
Distillation temperature, 50%	205.6°C	215.6°C	220.1°C
Distillation temperature, 90%	236.7°C	238.2°C	240.7°C

Experimental procedures and data analysis

The experimental procedure developed by the authors in the previous study [1] is modified to enable the characterization of CN on post injection retardability as follows:

1. For a given fuel, the engine is fired using the most advanced injection timings in the baseline injection calibration (A) for 20 minutes.
2. The desired injection strategy calibration is loaded into the engine control program. The main injection duration is adjusted to achieve the target load (3.25 bar of $IMEP_n$) within approximately 20 seconds.
3. After three minutes of steady-state engine operation, a measurement of 300 cycles of cylinder pressure data is taken, along with a one-minute average of emissions, temperatures, and fuel flow-rate data.
4. Steps 2 and 3 are repeated with block-shifting retardation of the two post injections in steps of 400 μs until the dwell between main and 1st post reaches 4695 μs, at which point hydrocarbon emission exceeds 500 ppm in most cases.
5. Steps 2-4 are repeated with injection calibration B, followed by calibration C.

6. The engine is stopped. The fuel system is flushed with n-heptane, purged with nitrogen, and filled with the next fuel. Steps 1–6 are repeated for each of the three fuels.

The data processing methodology used in this investigation is similar to that described in [1], so only the changes to these methods are described here. Closed-cycle energy balance analyses are applied to understand the flow of the fuel input energy. The defined time window for the analysis spans from intake valve closing (IVC) to exhaust valve opening (EVO). Thus, heat-loss and work are integrated over the closed portion of the cycle (IVC-EVO). Cumulative heat-release is integrated from the start of energizing of the 1st pilot until EVO. Blow-by is neglected.

The total input fuel energy for the closed-cycle analysis is expressed as the product of the injected fuel mass m_{fuel}, the fuel's lower heating value Q_{LHV} (given in Table 4) and the combustion efficiency computed from the exhaust gas measurements η_{comb}:

$$Q_{total} = m_{fuel}\, Q_{LHV}\, \eta_{comb}$$

(1)

The incomplete combustion loss is expressed as follows:

$$Q_{incomplete\ combustion} = m_{fuel}\, Q_{LHV}\, (1 - \eta_{comb})$$

(2)

The wall heat-loss Q_{wall} is computed according to Eqs. 3 and 4. $h_{Woschni}$ is the heat transfer coefficient as defined by Woschni [6], A_{cyl} is the surface area of the cylinder that varies with crank angle θ, T_{cyl} is the bulk gas temperature, and T_{wall} is the wall temperature, assumed to be 40°C, n is the engine speed in revolutions per second, B is the cylinder bore diameter, P is the measured cylinder pressure, S_{mp} is the mean piston speed, and P_{mot} is a calculated motored pressure. V_d is the engine's displacement volume; T_r, P_r, and V_r are the temperature, pressure, and cylinder volume at a reference point, taken as IVC for this work. C_1 and C_2 are tuning parameters that scale the velocity induced by piston motion and combustion velocity, respectively. C_m and C_2 are calibrated for each operating point to close the energy balance as described in [1]. The cylinder gas temperature at IVC is assumed to be 50°C in consideration of mixing with residual gas and heat exchange with combustion chamber walls before IVC. While the energy balance calculation is sensitive to this assumed temperature, the conclusions of the analysis are not, as long as the temperature at IVC can be assumed to be independent of fuel.

$$Q_{wall} = \int_{IVC}^{EVO} \frac{h_{Woschni} A_{cyl}}{n} \left(T_{cyl} - T_{wall}\right) d\theta$$

(3)

$$h_{Woschni} = C_m B^{-0.2} P^{0.8} T_{cyl}^{-0.546} \left[C_1 S_{mp} + C_2 \frac{V_d T_r}{P_r V_r}(P - P_{mot}) \right]^{0.8}$$

(4)

The exhaust heat $Q_{exhaust}$ is represented by the sensible enthalpy of exhaust gas at EVO $H_{exh}(T_{cyl,EVO})$ referenced to the enthalpy at 20°C, $H_{exh}(20°C)$. The enthalpy of the exhaust gas at these two

temperatures is calculated using the compositions of the exhaust gas at EVO, estimated based on the exhaust gas measurements and 6-term equations for themochemical data. Exothermic reactions that may occur in the exhaust port and runner are neglected.

$$Q_{exhaust} = H_{exh}(T_{cyl,EVO}) - H_{exh}(20°C)$$

(5)

The closed-cycle energy balance analysis is performed by two methods in this study. In the first method, exhaust heat is estimated with the assumption that the Woschni-correlated heat-loss calculation is valid; the available exhaust enthalpy is calculated by subtracting the incomplete combustion loss (Eq.2), the wall heat-loss (Eq. 3), and the closed-cycle boundary work from the total input energy (Eq.1). The second method is to calculate the wall heat-loss as the residual by subtracting the incomplete combustion loss (Eq. 2), the closed-cycle boundary work, and the exhaust enthalpy (Eq. 5) from the total input fuel energy (Eq. 1).

Eq. 5 is sensitive to the assumption of the bulk gas temperature at IVC, and inaccuracy in this assumed temperature appears to be the largest source of discrepancy between the two methods. However, the conclusions of this analysis hold regardless of the assumed temperature at IVC.

The exhaust heat flux (Φ_{ex}) in Eq. 6 [1] is calculated to represent the exhaust enthalpy that can be delivered to catalyst. It is normalized by the engine's displacement volume and expressed as follows:

$$\Phi_{ex} = \frac{c_{p,exhaust}(\dot{m}_{air} + \dot{m}_{fuel}) \Delta T}{V_d}$$

(6)

$c_{p,exhaust}$ is the specific heat of the exhaust gas, assumed to be 1.25 kJ/kgK. The total mass flow is computed excluding the portion of the simulated EGR, such that the heat flux is a measure of the enthalpy that would be available to heat the catalysts in the engine. ΔT is defined as $T_{exh} - 20°C$.

Numerical Simulations

Unburned hydrocarbons that are the result of incomplete combustion may be expected to form through multiple mechanisms, which include:

- Quenching of combustion reactions at the walls of the combustion chamber and due to expansion-driven cooling of the air-fuel mixture
- Incomplete combustion of overmixed (lean) mixture
- Incomplete combustion of undermixed (rich) mixture, including those associated with dribbled fuel [7]

Because fuel reactivity has been observed to primarily influence the ignition and combustion of the pilot injection, as well as unburned hydrocarbon emissions [1], it is hypothesized that the pilot mixture is an important contributor to engine-out hydrocarbon emissions. The relatively cool in-cylinder conditions result in long ignition delays that likely lead to overmixed conditions. On the other hand, the relatively short injection duration limits the momentum delivery into the cylinder and regions with undermixed conditions may also be

Page 5 of 18

expected. The potential for these two mechanisms to contribute to unburned hydrocarbon emissions is investigated with some simplifying assumptions and a low-fidelity modeling approach:

1. Only the 1st pilot injection is considered for this analysis. It is assumed that the fuel-air mixture formed from this injection is unchanged by ensuing injections.
2. A one-dimensional spray model is used to provide representative equivalence ratio distributions within a single spray and as a function of time under the experimental conditions.
3. At a given point in time relative to the start of the pilot injection, the mixture composition is frozen and discretized into parcels. The corresponding mixture temperatures are computed under the assumption of adiabatic mixing.
4. Each mixture parcel is subjected to a chemical kinetic computation with the initial temperature given by the mixing calculation. The measured cylinder pressure is imposed on the parcel, so the effects of compression heating of the mixture by the combustion are considered. No direct interactions between the mixture parcel and other reacting mixtures are considered.
5. For each parcel, the evolution of temperature and species concentrations are computed, as well as the final concentrations of hydrocarbons and formaldehyde (H_2CO) at the time of exhaust valve opening. H_2CO is an indicator of fuel-air mixture that has experienced first-stage, low-temperature reactions, but has not reached high-temperature ignition [8]. It is also an undesirable pollutant emitted from diesel engines [9].

The mixture formation process is simulated with the one-dimensional control-volume jet model proposed by Musculus and Kattke [10, 11]. This model predicts the spray behavior by solving mass and momentum exchange in multiple control volumes along the axial direction based on an assumed spray spreading angle and the measured rate of injection (ROI). The radial distribution of fuel is represented by a profile proposed by Abramovich [12] so a Lagrangian-type tracking of mixture parcel is not possible with this approach. However, this phenomenological model has been demonstrated to provide accurate predictions of mixture fields and spray penetration behavior [13, 14]. Thus, this modeling approach is deemed sufficient to output fuel-air mixtures that are representative of the conditions experienced by the single pilot injection.

Most of the tuning parameters are unchanged from their default values, as the model's purpose is only to generate representative mixture distributions. The nozzle diameter is taken as 0.150 mm, and the fuel density is 812.3 kg/m³. A 22° spreading angle is used. The maximum time step is set to 1 μs, and the Courant number is maintained below 0.2 during the simulation. The spray simulation is performed with an axial resolution of 0.05 mm and a radial resolution of approximately 0.01 mm. To obtain a selection of representative equivalence ratios, results are sampled with axial and radial resolutions of 0.8 mm and 0.16 mm, respectively. The two-dimensional depictions of mixture temperatures and air-fuel equivalence ratios shown in the Results section have been binned with this reduced resolution.

The rate of injection for the pilot injection is taken from a measured injection rate profile from the "A" injection schedule. Figure 3 shows the measured rate of injection (ROI) profile using Moehwald HDA for a single injector nozzle hole as a blue dashed line, and the ROI for the pilot injection only, which is used as an input to the jet model.

The timing of the pilot is held constant for every case; its duration is 0.23 ms, which is equivalent to 1.66 CA at 1200 rpm. The total injected mass of the 1st pilot is 1.89 mg.
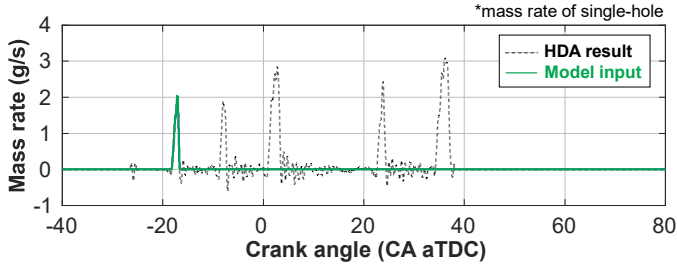

Figure 3: Injection mass flow rate profile used for simulation of a single spray. These curves have been produced by dividing the measured ROI profile by the number of injector nozzle holes (8).

The state of mixing is frozen at a given point in time relative to the start of injection. Then, an adiabatic mixing calculation is performed to compute the mixture temperature for each mixture parcel, assuming the fuel is fully vaporized. The adiabatic mixing temperature T_{mix} is calculated by solving the following equation, where ϕ is the equivalence ratio:

$$h_{gas}(T_{cyl}) - h_{gas}(T_{mix}) - \phi\left(\frac{F}{A_s}\right)\left(HoV + h_f(T_{mix}) - h_f(T_{fuel})\right) = 0$$

The initial fuel temperature (T_{fuel}) is set to the engine coolant temperature of approximately 310K. The bulk gas temperature at the moment the mixture distribution is frozen, T_{cyl}, is obtained from the combustion analysis. The enthalpy of the ambient gas, h_{gas}, is computed for the intake composition in Table 2 using 6-coefficient equations for ideal gases [15]. The stoichiometric fuel-air ratio $\frac{F}{A_s}$ is computed from the fuel properties listed in Table 4. The heat of vaporization (HoV) of the fuel is assumed to be equal to 360 kJ/kg. The sensible enthalpy of the fuel vapor, h_f, is computed using the relation given by Heywood in Table 4.11 [16]. Together with the newly calculated mixture temperature, the mixture composition and measured cylinder pressure define the thermodynamic state of each parcel.

Each mixture parcel is subjected to the measured cylinder pressure throughout the cycle while chemical kinetics are turned on. Thus, the effects of compression heating are considered. However, the effects of heat transfer between parcels, continued mixing, and direct interactions with subsequent injections are neglected. Parallel, closed system (control mass) computations are performed using the *ode15s* function in MATLAB to solve the following ordinary differential equations:

$$\frac{dT}{dt} = \frac{1}{mC_v}\left[-\sum_{species}\left\{\dot{w} \cdot V \cdot \left(\frac{h}{RT} - 1\right)\bar{R}\right\}T + \frac{1}{mC_v}\left[-P\frac{dV}{dt}\right]\right.$$

(8)

$$\frac{dV}{dt} = V\left[\left(1 + \frac{1}{P}\frac{dP}{dt}\right)^{-\frac{1}{\gamma}} - 1\right]$$

(9)

$\dot{w}$ is the net production rate for each chemical species [kmol/m³·s], h is specific enthalpy [J/kg], V is the parcel volume [m³], P is cylinder pressure [Pa], R is gas constant, $\bar{R}$ is the universal gas constant, and γ is specific heat ratio.

The Cantera 2.4.0 toolbox [17] is used in MATLAB to compute the chemical terms needed to solve Eq. 8 and the concentrations of each of the species of interest in the kinetic mechanism. Thermodynamic properties are obtained from Cantera's internal libraries. The computation begins when the ϕ-field is frozen and ends at EVO; the time step is set to 2 µs. The results presented in the following section are taken at EVO.

Two surrogate formulations for CN 45 and CN 55 have been created at Lawrence Livermore National Laboratory (LLNL) for use with the chemical kinetic computations to match specific properties of the CN45 and CN55 fuels. The composition of each fuel is optimized to match the CN, H/C ratio, and distillation characteristics shown in Table 4. An automated surrogate optimizer is used with a palette of normal and branched alkanes, as well as aromatics. The surrogate compositions for the CN45 and CN55 fuels are shown in Table 5:

Table 5: Surrogate fuel composition for chemical kinetic analysis. Values are mole fractions.

Compound	CN45	CN55
N-dodecane (n-$C_{12}H_{26}$)	22.77%	45.66%
N-cetane (n-$C_{16}H_{34}$)	2.54%	2.65%
Iso-cetane (heptamethylnonane)	9.33%	8.67%
A-methylnaphthalene (A_2CH_3)	8.33%	14.81%
Decalin ($C_{10}H_{18}$)	57.03%	28.22%

A detailed kinetic mechanism (unpublished) has been developed at LLNL to describe the ignition and combustion of these surrogate compounds. LLNL staff reduced the mechanism using the reaction flux analysis method and provided the reduced mechanism to support this work. The reduced mechanism has 343 species and 1941 reactions, and matches ignition delay predictions of the full mechanism over a range of conditions [18].

The evolution of formaldehyde, hydroxyl radical (OH), and unburned hydrocarbon (UHC) concentrations is tracked for each parcel, as well as the parcel's temperature.

10/19/2016

Results and Discussion

Engine experiments

Figure 4 shows the exhaust temperature plotted against indicated specific hydrocarbon (left column) and carbon monoxide emissions (right column) for each fuel and injection strategy calibration. For a given fuel, retarding the post injections typically increases unburned hydrocarbon and CO emissions while increasing exhaust temperature. A relatively short second post injection, as is the case with injection strategy C, increases pollutant emissions without a benefit of higher exhaust temperature. Increasing CN tends to simultaneously increase exhaust temperatures and reduce pollutant emissions, particularly for injection strategies A and B. In many cases, the sensitivity of exhaust temperature and pollutant emissions to CN is diminished as CN increases.
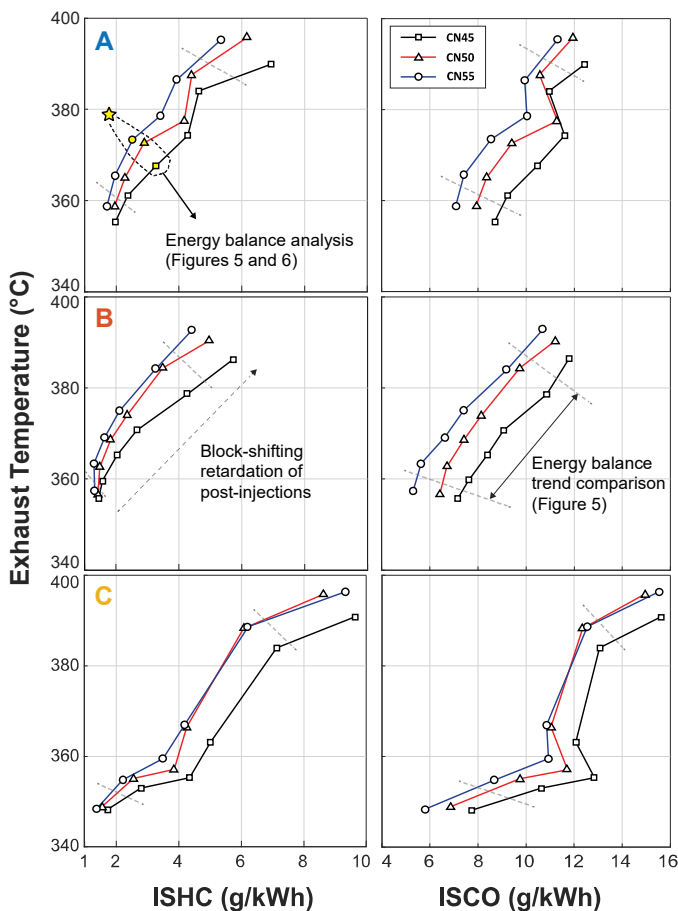
Figure 4: Tradeoffs between exhaust temperature and UHC/CO emissions. For a given injection strategy calibration, increasing CN tends to increase exhaust temperature and reduces pollutant emissions simultaneously. Some exceptions to this are observed for injection strategy C.

Figure 5 shows a comparative energy balance analysis for CN45 and CN55 under the conditions indicated in the second row and column of Figure 4. The bar plots show the difference in a calculated value with the CN55 fuel to its counterpart with the CN45 fuel. ΔE, shown at the top-left, represents the increase in supplied fuel energy needed to maintain load when changing from CN45 fuel to CN55 fuel. This

effect is more significant with calibrations A and B than with calibration C. $\Delta Q_{incomplete\ combustion}$ indicates the additional energy available from the more complete combustion of the CN55 fuel, as a consequence of the lower pollutant emissions shown in Figure 4. Wall heat-losses, as computed by the Woschni correlation (second row, first column) and by the residual method (second row, second column), indicate that the CN55 fuel results in higher wall heat-loss than the CN45 fuel. Finally, the bottom row of Figure 5 indicates that exhaust enthalpy is typically increased through the use of the CN55 fuel, as indicated by both the residual method (third row, first column) and the direct calculation method (third row, second column). The line plots shown in the third row represent an independent indication that the CN55 fuel results in higher exhaust enthalpy than the CN45 fuel.

The sensitivity of this analysis significantly relies on the accuracy of the fuel flow measurement. Flow fluctuations in the dual-loop fuel system shown in Figure 1 result in fluctuations in the fuel flow measurement of the Coriolis fuel flow meter that are not entirely compensated by time-averaging the results. This fluctuation, combined with the inherent inaccuracy of the fuel flow meter's calibration, provides an uncertainty on the order of 1-2%. The focus of the present analysis is on the change in exhaust enthalpy, which accounts for a few joules per cycle. Thus, the changes in exhaust enthalpy may be larger than what can be ascertained from the energy balance. Because of these limitations, the emphasis is not on the absolute accuracy of the values presented, but rather on explaining the trend of the result. However, it is noted that the change in exhaust heat flux, shown in the bottom two plots of Figure 5, is derived from the measurements of exhaust temperature, which is independent of the fuel flow measurement. Despite the different methodology, both indicate that the use of CN55 fuel increases exhaust heat.
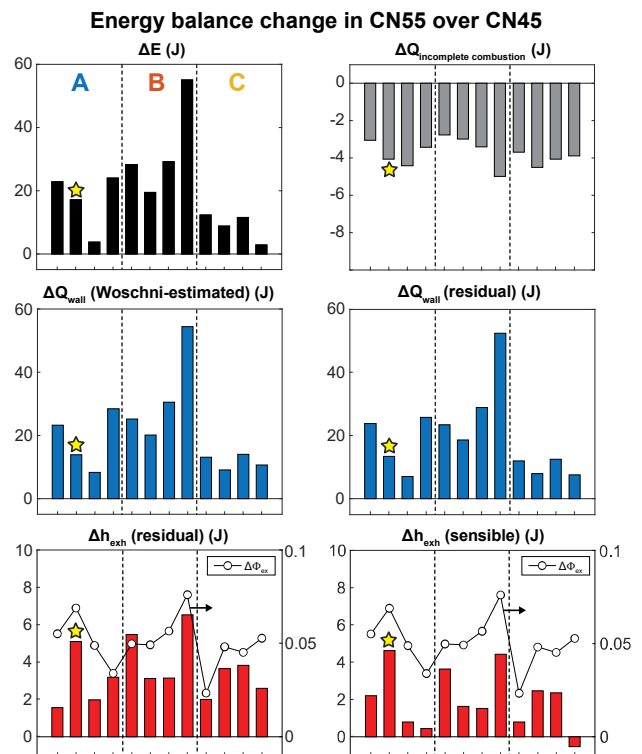

Figure 5: Change in per-cycle energy balance analysis with CN55 fuel referenced to CN45 for the operating points indicated in Figure 4. The emphasis is the relative trends as the CN is increased from 45

10/19/2016

Figure 6 shows more detailed energy balances for a representative operating point shown with the star markers in Figure 4 and Figure 5. Two stacked bars are shown for each fuel and correspond to the two methods used to perform the energy balance as described above. For each fuel, the left stacked bar shows the exhaust heat when calculated as the residual, and the right group shows the wall heat-loss as the residual of the calculation.
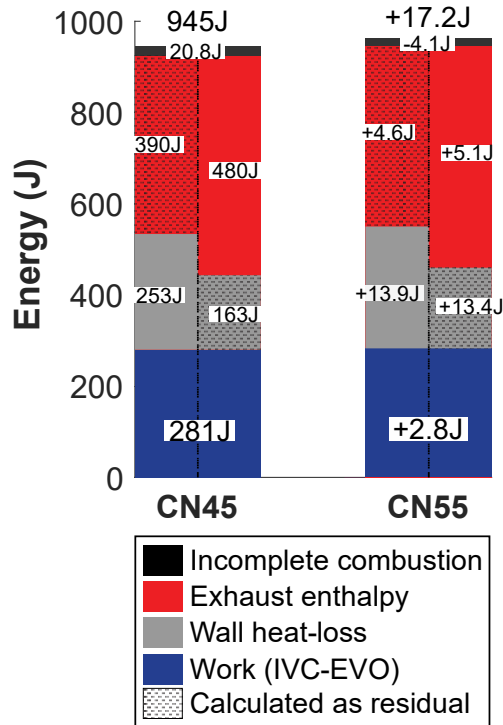

Figure 6: Energy balance analysis for the operating point indicated with the star markers in Figure 4 and Figure 5. The emphasis is not on the absolute accuracy of the energy balance, but rather on the relative trends as the CN is increased above 45. These trends are relatively insensitive to the assumptions and uncertainties inherent in this analysis.

With the CN55 fuel, an increase of 17.2 J (relative to the CN45 baseline) in fuel energy is necessary to maintain the load. Combustion losses are 4.1 J lower than with the CN45 fuel. A significant increase in wall heat-loss is estimated with both energy balance methods and is the primary reason for the increased fueling requirement. Because a significant fraction of the fuel energy ends up as exhaust heat, the increase in fueling necessarily increases the exhaust enthalpy. However, the proportion of exhaust loss relative to fuel energy input is lower as a result of the higher wall heat-loss: 41.0% (left) and 50.4% (right) compared to those of CN45, which are 41.3% (left) and 50.8 (right).

In summary, increasing CN results in more complete combustion. However, it results in a more substantial increase in wall heat-loss, so additional energy input and fuel mass are required to maintain the load. Part of the additional fuel input is converted to exhaust enthalpy, which leads to increased exhaust temperatures. The proportion (not the absolute value) of the fuel conversion available

for the exhaust enthalpy decreases due to increased wall heat-loss, implying that higher CN fuel may facilitate faster catalyst heating as well as a reduced engine warm-up period. An optimized calibration of injection timing may provide a better utilization of fuel conversion to exhaust enthalpy [3].

In-cylinder pressures for the selected condition are shown in Figure 7 for three different fuels, and the injection current signal is also indicated with a green line. Due to long ignition delays at the lower pressure and temperature conditions of catalyst-heating operation, the fuel delivered by the 1st pilot injection does not react until the SOE of the 2nd pilot injection, regardless of fuel CN. High-temperature heat-release occurs after the 2nd pilot injection, a clear influence of the CN is observed during the combustion after the 2nd pilot and main injections, and higher CN leads to faster pressure build-up. After the combustion associated with the main injection, the difference between the three fuels diminishes, and eventually the pressure profiles are almost identical after 10 crank angle degrees after top dead center (CA aTDC).
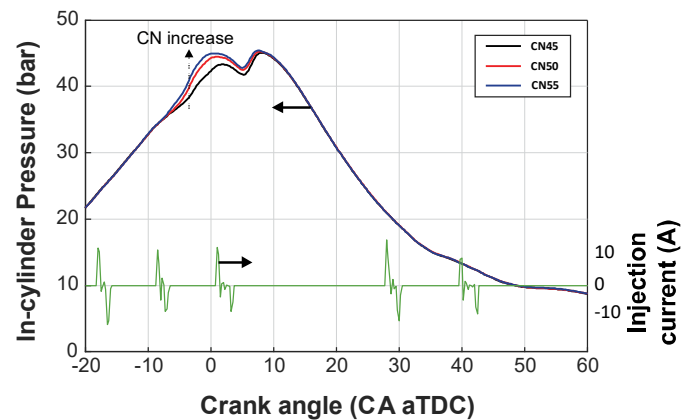

Figure 7: Cylinder pressure curves for the operating point indicated with the star marker in Figure 4 and Figure 5. CN affects the portion of the pressure trace associated with combustion that occurs well before the post injections.

Figure 8 illustrates the heat-release rate and cumulative heat-release curves, including wall heat-loss plotted against crank angle. These curves confirm that the combustion associated with the two post injections are not significantly affected by the fuel change. Instead, the fuel CN primarily affects the heat-release behavior of the pilot combustion. This trend is found in most of the different injection calibrations and timings in this study (the operating points in Figure 4), and is well-aligned with the findings of the previous study [1]. Increased CN primarily results in a more advanced, intense heat-release of the pilot mixture. While increasing the CN, MFB10 (10% mass fraction burn point) is gradually advanced from 3.79 CA aTDC at CN45, to 0.31 CA aTDC at CN50, and to 0.95 CA bTDC at CN55. Observing other burn points later than MFB10 show very subtle variations, and do not show meaningful change due to the similarity in heat-release rate in later phase.
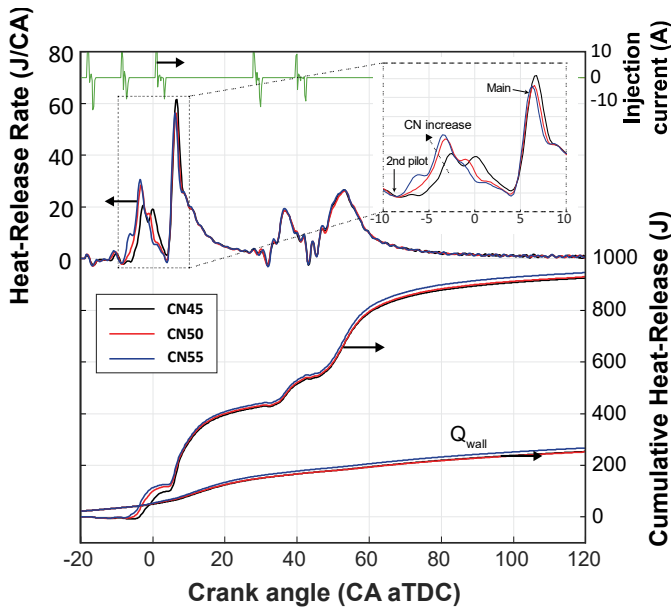
Figure 8: Heat-release rate, cumulative heat-release, and cumulative wall heat-loss plotted against crank angle for the operating point indicated by the star marker in Figure 4 and Figure 5. Remarkable difference is found in heat-release associated with the pilot and main injections, whereas combustion of the post injections is almost identical for all three fuels.
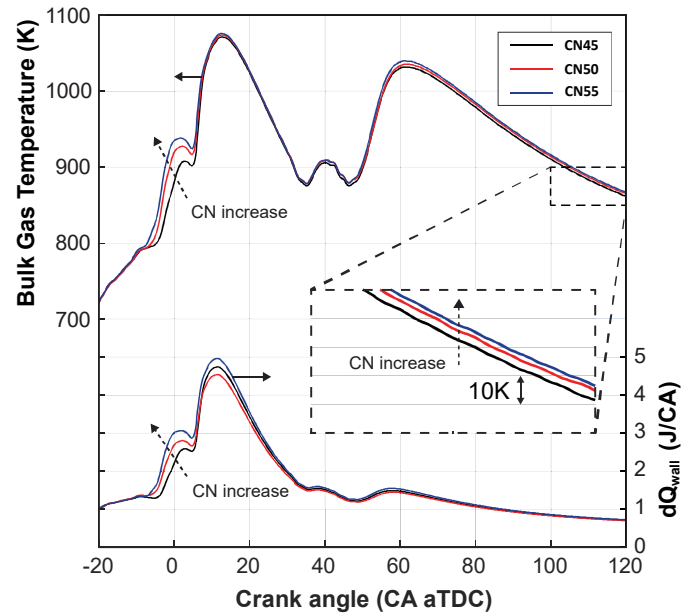

Figure 9: Bulk gas temperature and rate of wall heat-loss plotted against crank angle for the operating point indicated by the star marker in Figure 4 and Figure 5. The effect of fuel CN on both plots are most pronounced during the initial stages of pilot heat-release. Trends in bulk gas temperature at EVO correspond to the exhaust temperature behavior shown in Figure 4.

Some changes are also observed in the peak of heat-release rate associated with the main injection: the less reactive CN45 fuel has the highest peak heat-release rate despite having the lowest main injection quantity and the lowest fueling amount. It is believed that the fuel delivered by the pilot injections does not burn completely before the main injection, and some reactions may occur during the combustion associated with the main injection. This is consistent with the delayed heat-release of the pilot mixture. The higher peak heat-release rate for the CN45 is consistent with the faster pressure rise during the main combustion. The larger fuel quantity required with the CN55 fuel results in very subtle differences in heat-release, but it is apparent in the cumulative heat-release plots: this difference begins to be observed during the late part of the main heat-release event.

Bulk gas temperature and rate of wall heat-loss are plotted against crank angle in Figure 9. The three different fuels exhibit no significant difference in the gas temperature until the 2nd pilot injection. The 1st pilot injection does not develop into an immediate and rapid reaction in catalyst-heating operation, even with the highest CN fuel. Strong interactions between two sequential injections have been found in previous research in a spray chamber under catalyst-heating operation-like conditions [19], and the study also suggested that the 1st pilot injection is highly unlikely to ignite rapidly at such cold conditions. Rather, the mixture formed by the 1st injection experiences low-temperature reactions, but high-temperature reactions occur when the mixture from the 2nd injection catches up to that of the first injection and enriches it. An earlier temperature rise is shown for higher CN fuels. Second-stage ignition occurs for all three fuels during the combustion of the 2nd pilot injection, with CN55 showing the faster temperature rise rate.

The temperature increase during the pilot and main combustion plays an important role in determining the total wall heat-loss. The earlier, more robust phasing of the first high-temperature reactions results in the higher bulk-gas temperatures, which increase the wall heat-losses for the more reactive fuel. The bulk gas temperatures computed near EVO show a good agreement with the trends in measured exhaust temperatures: increasing CN increases bulk gas temperatures but with diminishing gains. The overall increase between the CN45 and CN55 cases is between approximately 5 and 10K.

As expected, the wall heat-loss rate is significantly increased with the CN55 fuel during the pilot and main combustion periods. However, the heat-loss behavior during the main combustion is not so intuitive. The relative magnitudes of wall heat-loss are not correlated well with the bulk gas temperatures; the CN50 fuel results in the lowest rate of wall heat-loss despite the slightly increased bulk gas temperature compared to the CN45 fuel. The difference in the heat-release rate profiles during the main combustion are attributed to changes in the tuning of the coefficient C_2 in the Woschni model. One possibility is that the higher peak heat-release rate for the CN45 (Figure 8) is responsible for a 13% higher value of C_2 for the CN45 fuel, and thus the predicted wall heat-loss is slightly higher during the main combustion. In Eq. 4, the term that includes C_2 generally represents the response of heat transfer coefficient to the combustion of the in-cylinder gas mixture. The effects of the higher cylinder-pressure rise rate during the main combustion of CN45 may therefore be incorporated in the heat transfer coefficient. However, this mechanism has yet to be conclusively demonstrated; a further study including experimental heat transfer measurements will provide data needed to evaluate this hypothesis.

Differences in the bulk gas temperature and wall heat-loss are observed during the combustion of post injections as well. However, overall wall heat-loss rates are much lower during this phase than

during the main combustion, so the contribution of these effects to total cumulative heat-loss is relatively small; it is believed that the behavior during the combustion of the pilots and the main injections are responsible for the changes in wall heat-loss that degrades the thermal efficiency and increase fueling requirements.

The increased wall heat-loss is typically undesirable because of its negative impact on thermal efficiency. However, for the catalyst-heating operation, the higher heat-losses increases the fueling required to maintain the load, which provides additional energy to the exhaust. Further, the increase in heat addition to the coolant via increased wall heat-loss may be beneficial for thermal management of the engine and passenger compartment during cold starting.

The energy balance and heat-release analyses indicate that the most apparent result of increasing CN appears to be the more robust combustion of the pilot mixture. The experimental evidence is largely consistent with the expectation that the more robust combustion increases wall heat-loss and thus the fueling required to maintain the load. This increase in fueling necessarily results in an increase in exhaust enthalpy. On the other hand, the reductions in UHC and CO emissions (see Figure 4) that accompany the increase in CN are still not fully understood. The former of these is the focus of the continued analysis.

Numerical simulations of mixture formation and chemical kinetics

Figure 10 shows the predicted distribution of fuel-air equivalence ratio, ϕ, for crank angles from the top (17 crank angle degrees before TDC (CA bTDC) to the bottom (16 CA bTDC). The horizontal axis indicates the distance from the injector tip, which is located at the origin of each of the axes. The direction of spray penetration is from left to right. For the purposes of this analysis, the mixture distribution

is frozen at 16.4, 16.2, and 16.0 CA bTDC, which are represented in the three bottommost plots in Figure 10.
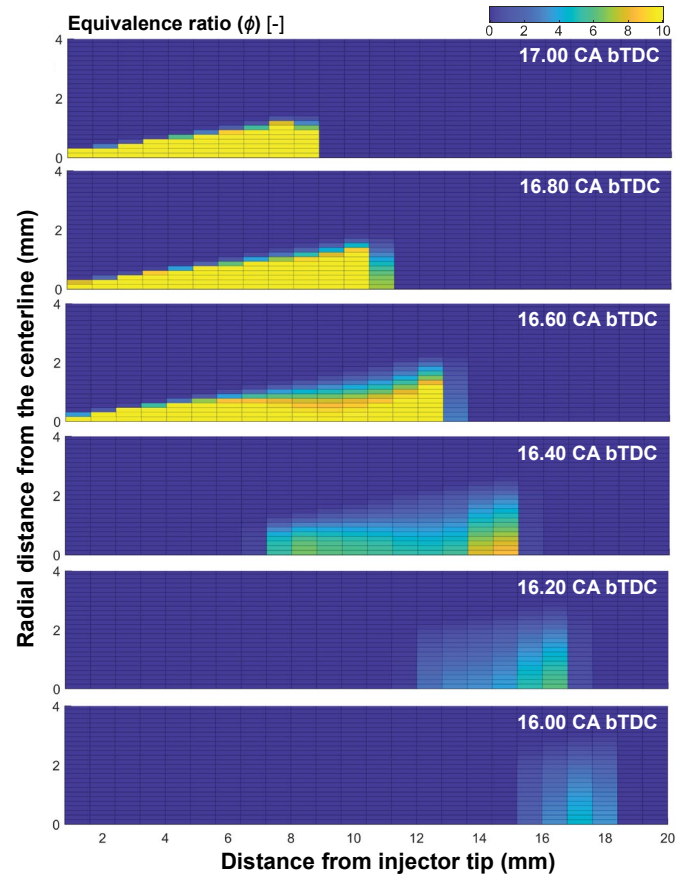

Figure 10: Predicted fuel-air equivalence ratio distributions for the 1st pilot injection at various times. Injection begins shortly before 18 degrees bTDC, and ends shortly after 17 degrees bTDC.

Figure 11 shows the computational results for the CN45 fuel when the mixture composition is frozen at 16.2 CA bTDC. The ϕ distribution and initial temperature field are shown on the two topmost plots. Rich mixtures exhibit the lowest temperatures because of the lower amount of air entrained and the larger energy required to vaporize the larger mass of fuel. On the other hand, the highest temperature is observed near the spray boundary for the leaner mixtures.
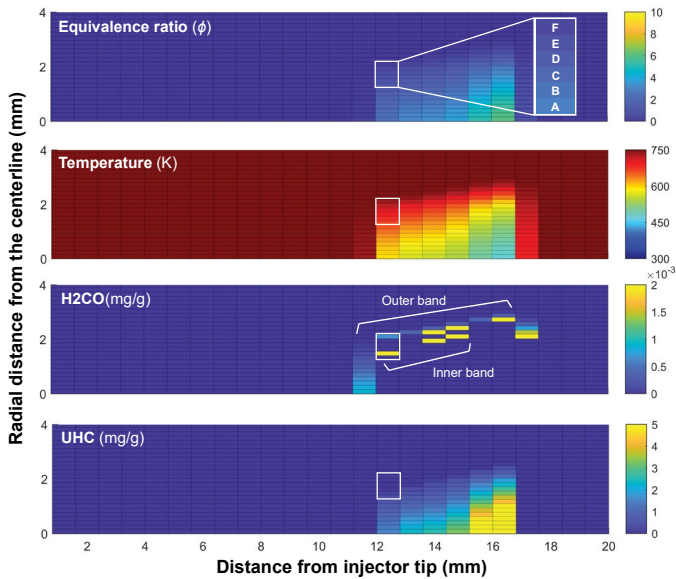
10/19/2016

Figure 11: Equivalance ratio (top) and mixture temperature (second from top) distributions predicted by the 1D spray model at 16.2 CA bTDC for the CN 45 fuel. The bottom two images show the distributions of H_2CO and UHCs that exist at EVO after these mixtures have been allowed to react while subjected to the measured cylinder pressure trace.

The third image in Figure 11 shows the mass fractions of H_2CO remaining at EVO for each mixture parcel, with each mixture parcel having been subjected to the measured cylinder pressure trace for the operating point indicated by the star marker in Figure 4 and Figure 5. H_2CO frequently persists in mixtures originated around the spray periphery (referred to as the "outer band"), where equivalence ratios are relatively low and initial temperatures are higher than in the richer mixtures nearer the spray centerline. H_2CO is also predicted to form in a second region (inner band) that is further inboard. The image at the bottom indicates that UHC emissions are not fully consumed in the rich mixtures that exist in the interior of the spray. A white box indicates the positions of six mixture parcels (labeled A-F), that are analyzed in detail. Mixture parcels C and F exist in the inner and outer bands, respectively, and are the only two that result in significant amounts of H_2CO at EVO.

Figure 12 shows the temporal evolution of temperature and mass fraction of key species for each fuel parcel highlighted in Figure 11. On each line plot, the mass fractions of various species, namely fuel, UHC (including fuel), H_2CO, and OH, as well as temperature are plotted against crank angle. The parcel designation (A–F) is shown at the top-left of each plot. For parcel A, the initial mixture temperature is too low for reactions to occur, resulting in a high mass fraction of unburned fuel. The lack of reaction is observed in all of the parcels in the interior of the spray (inner band) that are emphasized in the bottom image in Figure 11. In reality, the mixing process continues unlike the assumption of frozen state made in the simplified analysis. Thus, continued spray penetration and fuel-air mixing may be expected to promote heating and ignition of this fuel in the experiments.

For parcel B, ϕ and the calculated initial temperature are 0.914 and 679 K, respectively. As indicated in Figure 11, this mixture results in a significant amount of H_2CO remaining at EVO. The plot shows that very little fuel is consumed before 20 CA aTDC, after which low-

temperature heat-release (LTHR) is predicted as first-stage ignition occurs. The fuel and UHC fractions decrease, a considerable amount of H_2CO is formed, and the temperature rises due to the LTHR. However, the mixture is not predicted to experience complete second-stage ignition, despite reaching temperatures exceeding 950 K late in the cycle. The relatively low cylinder pressure and fast expansion of the cylinder volume at this late stage likely inhibits and/or quenches high-temperature ignition. This is an example of what can happen to mixtures in the "inner band" indicated in Figure 11. Results of engine experiments suggest that, under some conditions, a portion of the mixture attributed to the pilots and the main injection can react very late in the cycle [1].

The mixture in parcel C has a lower fuel concentration, ϕ is 0.726, and thereby initial temperature is approximately 13 K higher than that of mixture parcel B. Due to the higher initial temperature, the first-stage ignition is advanced, and the second-stage ignition follows within 5 crank angle degrees. The fuel is mostly consumed by the first-stage ignition, which results in significant H_2CO formation. The sudden appearance of OH radicals shortly after the disappearance of H_2CO indicates high-temperature ignition, which results in temperatures exceeding 2000 K. Combustion reactions proceed close to completion, and essentially no UHCs or H_2CO remain at EVO.

The initial equivalence ratio continues to decrease for parcels D and E. Thus, the initial mixture temperatures increase and first-stage ignition occurs sooner. Reaction temperatures remain sufficiently high for the second-stage ignition, but the decreasing fuel concentration extends the delay between first- and second-stage ignitions.

As ϕ decreases further, as in parcel F, the increased mixture temperatures continue to advance first-stage ignition. However, first-stage reactions are not exothermic enough to reach the temperature required to initiate second-stage reactions (see, for example, [20]), so second-stage ignition does not occur despite the considerable increase in the initial temperature. H_2CO formed during first-stage ignition persists until EVO, which results in the "outer band" regime shown in Figure 11.

In summary, the first-stage ignition of the fuel-air mixture resulting from the 1st pilot injection is more sensitive to the temperature of the mixture than to its equivalence ratio. Mixtures that are richer than stoichiometric may not have sufficiently high temperature to reach the first stage ignition, and could contribute to UHC emissions if turbulence-chemistry interactions and/or interactions with other injections fail to change this. H_2CO and other products of incomplete combustion that form by low-temperature reactions persists until EVO by two mechanisms:

1. Outer band: first-stage ignition occurs relatively quickly due to elevated mixture temperatures, but the amount of heat released is insufficient to initiate second-stage ignition and the intermediate species are not fully oxidized. In reality, turbulent transport of these intermediate species into richer mixtures in the interior of the spray (see, for example, [21]) would advance first-stage ignition in those mixtures and could therefore increase the probability of their second-stage ignition. The heat produced from those reactions could potentially heat the leaner mixtures in the outer band and help to reach second-stage ignition. On the other hand, further air/fuel mixing would decrease the mixture's equivalence ratio, which would likely hinder second-stage ignition. The ultimate impact of these mixtures on engine-out UHC emissions is unknown, but the

relatively small amounts of fuel contained in these leanest mixtures may limit their contribution.

2. Inner band: while the equivalence ratios in this region are in the ignitable range, the limited amount of air entrained, which results in the lower mixture temperature, leads to delayed first-stage ignition. Low pressures during the expansion stroke may further hinder the second-stage ignition. Such mixtures will persist until EVO unless a) turbulence-chemistry interactions transport intermediate species from the outer band into the inner layer of the spray and promote low-temperature chemistry, as described above, or b) there is a more direct interaction with the subsequent injections that promotes further air entrainment and/or provides direct, localized heating that promotes the second-stage ignition. Swirl motion in the cylinder could transport some of the mixtures from the 1st pilot to locations where such interactions with subsequent injections are not possible. This is one hypothesized mechanism by which undermixed fuel from the 1st pilot injection could contribute to UHC emissions in the exhaust. However, the kinetic mechanism is extremely sensitive to initial conditions, as well as variations in the pressure-temperature trajectory of these mixtures. This fact, combined with the factors mentioned above, increases the probability of second-stage ignition that would diminish the impact of these mixtures on engine-out UHC emissions.
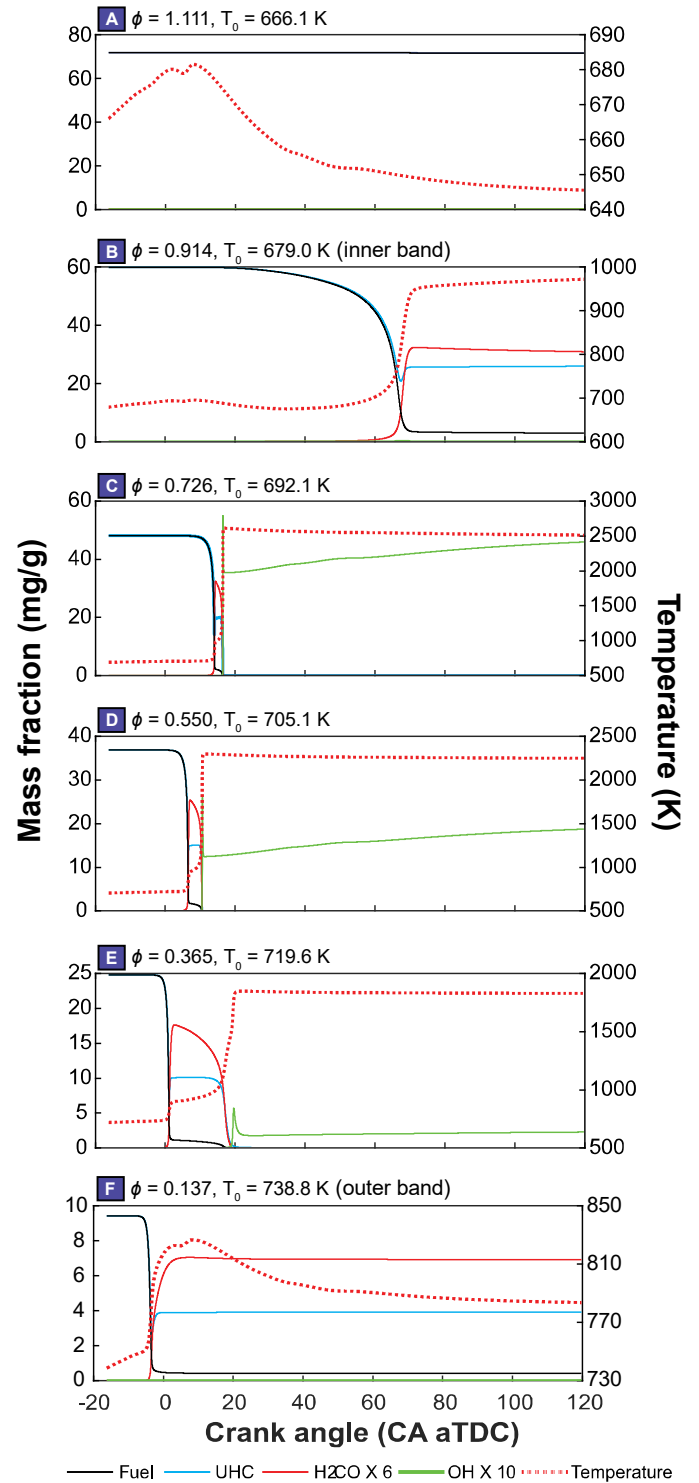

Figure 12: Results of chemical-kinetic simulations for the mixtures shown in Figure 11 for the CN45 fuel. H_2CO and UHCs can be produced in lean mixtures and in near-stoichiometric mixtures that reach first-stage ignition very late.

Figure 13 shows the spatial distribution of H_2CO and UHC mass fractions at EVO for the CN55 fuel based on the frozen mixture composition at the same timing as for the CN45 fuel (16.2 CA bTDC). Comparison between Figure 11 and Figure 13 reveals that increasing the CN shrinks the region with high UHC levels arising

from the unreacted fuel in the spray's interior. Furthermore, the inner band of H_2CO emissions is no longer predicted; the higher CN effectively promotes second-stage ignition in these mixtures. However, much of the H_2CO that originates in lean mixtures on the spray periphery persists. Even for the more reactive fuel, it fails to achieve the second-stage ignition in these lean mixtures, as temperatures are still too low to initiate the second-stage chemistry.
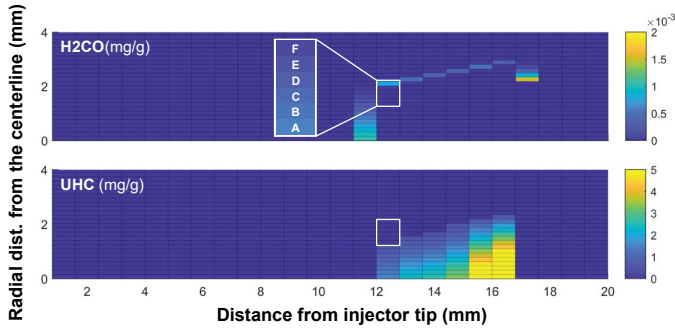

Figure 13: Distributions of H_2CO and UHCs predicted at EVO for the CN55 fuel. The mixture field is frozen at the same crank angle (16.2 CA bTDC) and subjected to the same cylinder pressure trace as for the results in Figure 11.

Figure 14 shows the temporal evolution of temperature and mass fraction of key species for the CN55 fuel. The simulation results are obtained for the parcels that correspond to those referenced for the CN45 fuel (see Figure 11). The mass of fuel and air in each parcel are considered the same for both the CN45 and CN55 fuels. Because the heat of vaporization of the two surrogates were assumed identical, the initial temperature of the mixture is also identical for the two cases. However, due to the slightly different H/C ratio of the surrogate formulations of these two fuels, the equivalence ratio in each parcel is different. Additional simulations where identical equivalence ratios are prescribed have also been performed, but those results (not shown for brevity's sake) do not alter the findings presented here.
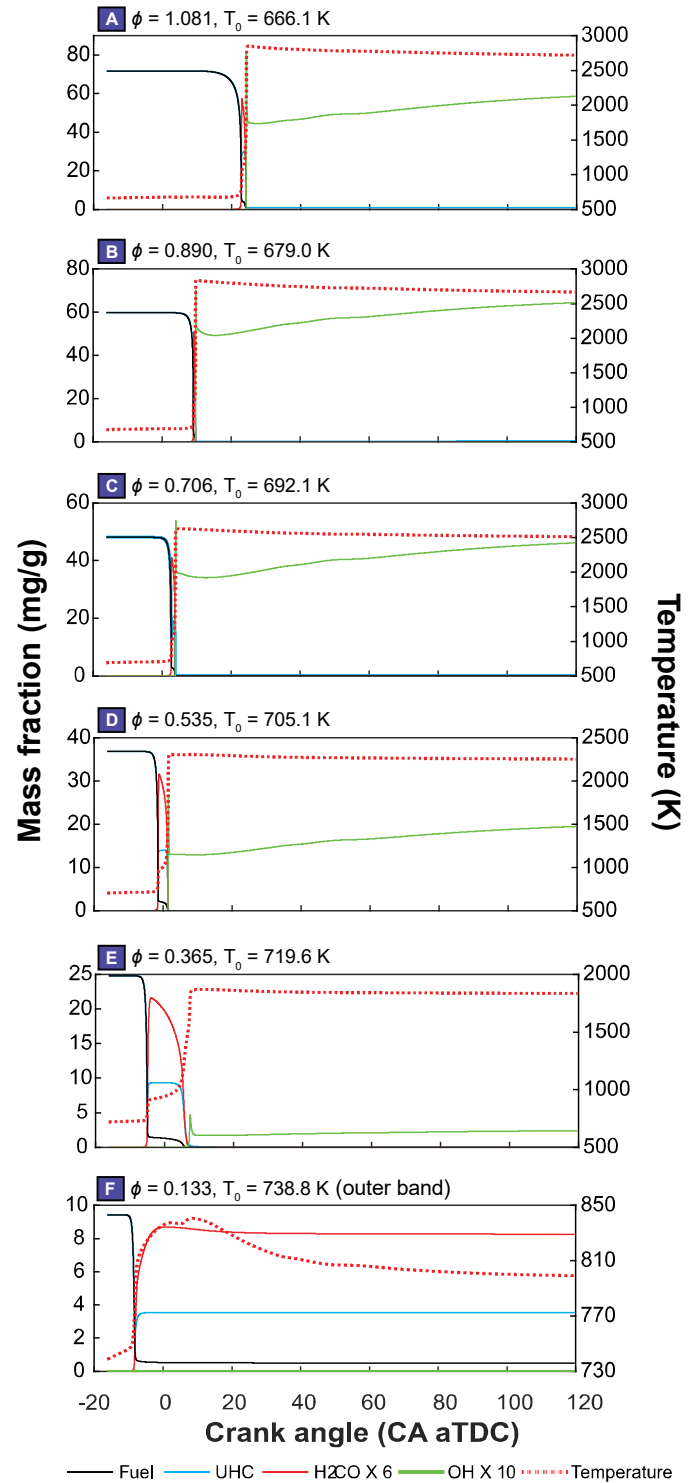

Figure 14: Results of chemical-kinetic simulations for the mixtures shown in Figure 13 for the CN55 fuel. The increase in CN promotes second-stage ignition of mixtures in the spray's interior, but not in the lean outer band (mixture F).

The CN55 fuel advances the timing of first-stage ignition regardless of the equivalence ratio and initial mixture temperature, as compared to CN45 (see Figure 12). With the CN45 fuel, no reactions are predicted to occur for parcel A. In contrast, the corresponding CN55 mixture parcel exhibits first-stage ignition, followed shortly by
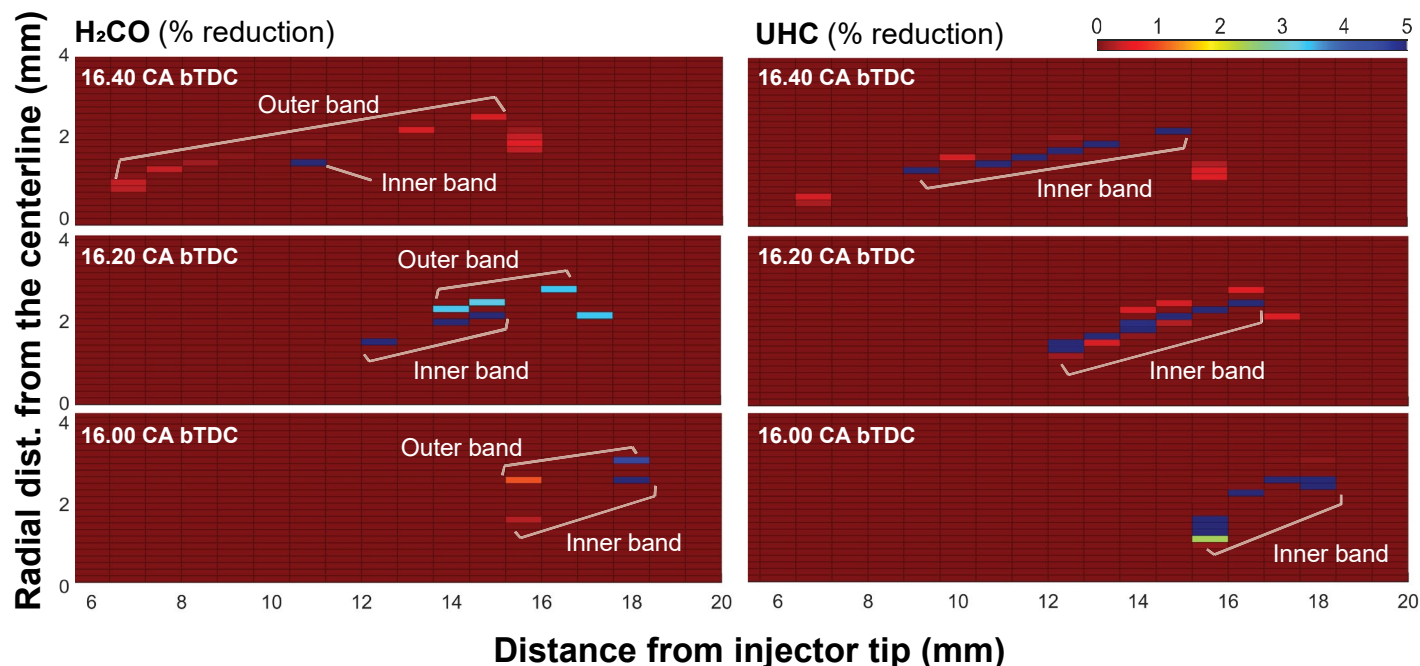
Figure 15: Relative changes in H₂CO (left column) and UHC (right column) at EVO when changing from CN45 fuel to CN55 fuel with mixtures frozen at three crank angles: 16.4 CA bTDC, 16.2 CA bTDC, and 16.0 CA bTDC. The changes are normalized so that the sum of all changes in a given image is 100%.

second-stage ignition. This results in complete oxidation of hydrocarbon species and is the reason for the smaller region of unreacted fuel in Figure 13 compared to that shown in Figure 11. In the lean mixtures found in the outer band, the exothermic first-stage reactions are still unable to elevate temperatures to the degree needed to initiate second-stage ignition. Overall, increasing the CN increases the amount of mixture that achieves second-stage ignition. This is consistent with the experimental results showing reduced UHC emissions with the CN55 fuel, compared to the CN45 fuel. However, it is important to note that this simplified analysis cannot provide a complete understanding of the behavior shown in Figure 4, as it neglects interactions with the mixtures that form from the 2nd pilot, main, and post injections.

Figure 15 shows the reduction percentage of both emission components at CN55 fuel compared to CN45 fuel. The left column shows the reduction in the normalized percentage of H₂CO (the percentages shown in the figure add up to 100%) and the corresponding reductions in UHC are shown in the right column. Each row corresponds to a different time at which the initial mixture composition is frozen: either at 16.4, 16.2 or 16.0 CA bTDC. As discussed previously, some H₂CO reduction is observed in the outer band, but the most significant portion of the reduction in H₂CO occurs in the inner band. Additionally, the UHC reduction in the inner band is most significant and is attributed to the higher probability of mixtures of CN55 to achieve high-temperature heat-release (HTHR). Recall that the fuel distributions are biased toward the interior of the spray (see Figure 10), so that the mixtures in the inner band can contribute more to the total mass of unburned hydrocarbons than do the mixtures in the outer band.

As described above, the reaction of the inner band is highly sensitive to the P-T trajectory to which the mixture in each parcel is subjected. These effects are investigated with simulations using the in-cylinder pressure profiles from different injection strategy calibrations with the CN45 fuel. Figure 16 shows the pressure traces from three

different degrees of block shifting of the post injections. The solid black line indicates the reference case that has been used as the pressure input for the results shown above, and for the baseline case of energy balance analysis. The blue dashed line is the pressure trace associated with the most advanced injection timing among "A" injection calibrations, which has the lowest exhaust temperature. The red dashed line is the "A" calibration with the highest exhaust temperatures and the most retarded phasing of the block-shifted post injections. Differences in the cylinder pressure associated with the main injection are attributed to the changes in the main injection duration to maintain the load with the changes in the phasing of the post injections.
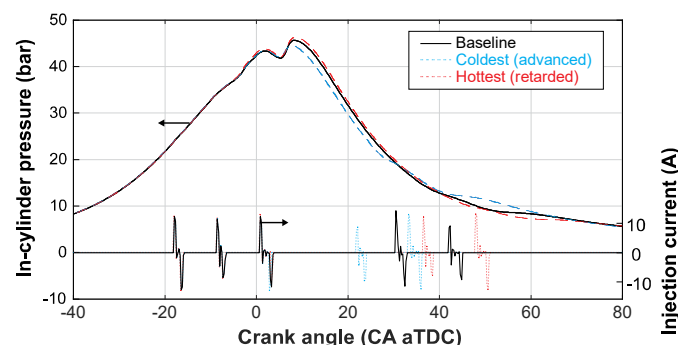

Figure 16: Pressure traces used for additional kinetic simulations. The post injections have been block-shifted and the main injection quantity has been adjusted to maintain load. The resulting changes in the cylinder pressure trace correspond to different P-T trajectories to which the pilot mixture is subjected.

Figure 17 shows the H₂CO produced from the mixtures subjected to the two alternative pressure profiles, using the mixture distribution frozen at 16.2 CA bTDC. The top plots in both (a) and (b) show the distribution of H₂CO at EVO, and their bottom plots indicate the

mass fractions and temperature of the reactions of the white-ellipsed parcels in the inner band. The chemistry of the inner band shows a strong sensitivity to the subtle changes in the pressure (and temperature) profile. The retarded injection calibration, i.e. (b), accompanies additional fueling in the main injection to compensate for the decrease in load resulting from the more retarded combustion phasing. Thus, higher pressures and temperature prevail during the main combustion with the most retarded injection strategy. A higher degree of compression heating is therefore applied to the mixture, which accelerates both first- and second-stage ignition, effectively reducing H_2CO and UHC. As mentioned above, this sensitivity to the P-T trajectory increases the probability that local interactions with subsequent injections will promote second-stage ignition in these mixtures, thus reducing their contribution to engine-out UHC emissions. Turbulence/chemistry interactions within the mixture would also be a source that makes this mechanism less likely to survive, as it can quickly induce low-temperature chemistry.
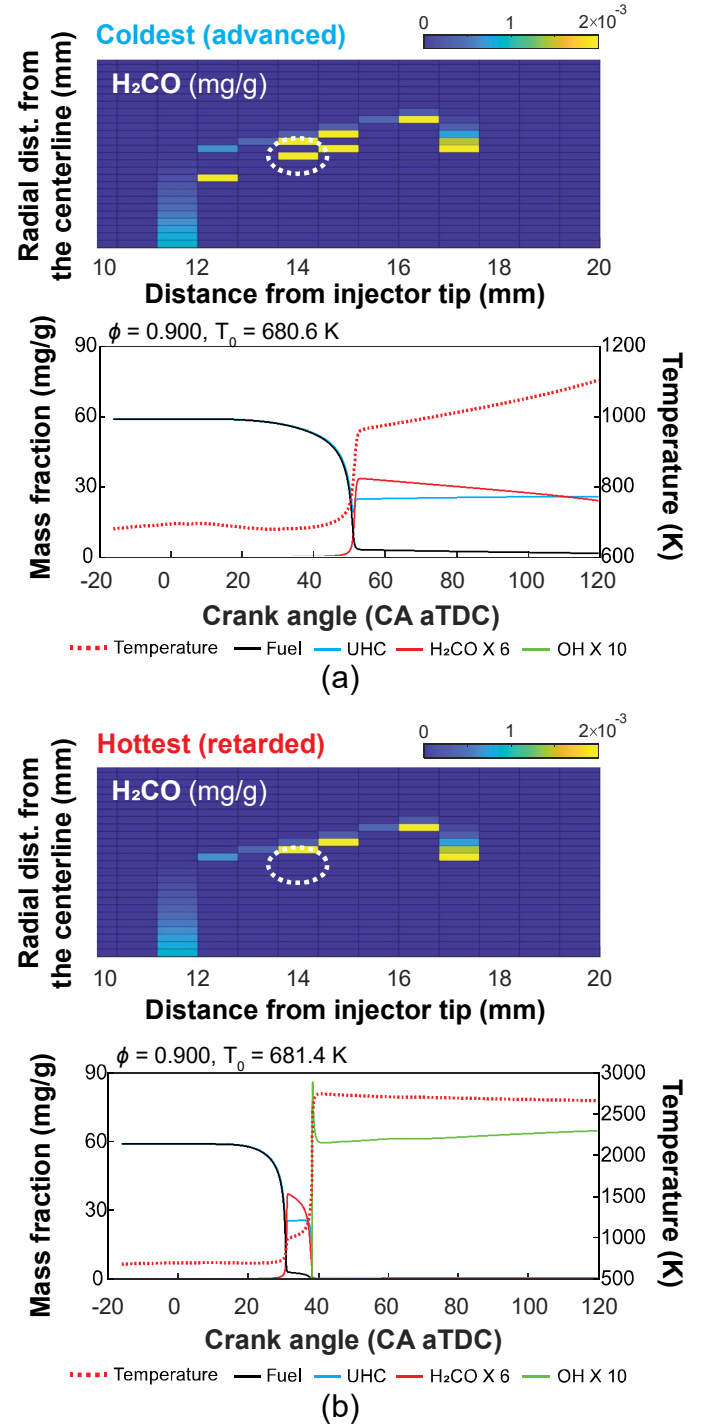

(a)

(b)

Figure 17: Distributions of H_2CO predicted at EVO for the CN45 fuel under the influence of two alternative cylinder pressure profiles (top of each plot). Results of chemical-kinetic simulations for the mixtures shown by the ellipses (bottom of each plot). The differences in the pressure trajectory result in dramatically different outcomes.

The H_2CO formation in the outer band zone is relatively insensitive to changes in thermodynamic conditions and is not significantly affected by the two alternate pressure traces. This strongly implies that the mixtures in the periphery of the 1st pilot injection spray may be an important contributor to engine-out H_2CO and UHC emissions.

10/19/2016

Summary/Conclusions

The mechanisms by which the cetane number of the fuel influences the thermodynamic performance and pollutant emissions during catalyst-heating operation have been investigated in a single-cylinder medium-duty diesel engine. Three injection strategies were developed, for which the post injections were block-shifted to retard combustion phasing. Experiments were performed with three fuels with different cetane numbers (CN45, CN50 and CN55). Detailed thermodynamic analyses provided insight into how cetane number affects exhaust temperatures. Low-fidelity spray modeling was coupled with chemical kinetic simulations to investigate potential mechanisms by which the 1st pilot injection may contribute to formaldehyde and unburned hydrocarbon emissions in the exhaust. These analyses support the following conclusions:

1. Increasing cetane number reduces unburned hydrocarbon emissions and increases exhaust temperatures for a given injection strategy calibration. For a given unburned hydrocarbon emission level, an increase in the cetane number from 45.3 to 54.3 can increase exhaust temperatures by approximately 5 to 10 K, depending on the calibration and the unburned hydrocarbon emission level.
2. The use of higher cetane number fuel tends to increase wall heat-losses due to higher temperatures resulting from more advanced, robust pilot combustion. Heat-release associated with post injections is essentially unaffected by cetane number, in agreement with previous studies.
3. As the cetane number increases, more fuel is required to maintain the load due to the increasing heat losses, which necessarily increases the exhaust enthalpy. This appears to be the primary mechanism by which higher cetane fuels increase exhaust temperature for a fixed calibration.
4. Formaldehyde can form in fuel-air mixtures resulting from the 1st pilot injection and persist until exhaust valve opening by two mechanisms:
   a. The failure of low-temperature reactions in the lean mixtures near the spray periphery to increase local temperatures enough to initiate high-temperature reactions. This mechanism persists for all investigated perturbations in mixture composition, temperature, pressure trajectory, and fuel cetane numbers. The extent to which these mixtures avoid direct interaction with reacting mixtures from subsequent injections will determine their contribution to engine-out formaldehyde and unburned hydrocarbon emissions associated with the pilot injection.
   b. A significant amount can form in rich mixtures in the interior of the pilot mixture, as a result of prolonged first-stage ignition and failure to reach second-stage ignition. However, this mechanism is less likely to survive due to its sensitiveness to change in thermodynamic conditions.
5. With higher cetane number fuel, reduction in unburned hydrocarbon emission associated with 1st pilot injection is mainly attributed to the enhanced chemical reactions that allow the high-temperature heat release of rich spray mixtures. This portion is a part of the total reduction of unburned hydrocarbon emission during the operation.

References

1. Busch, S., Wu, A., and Cho, S., "Catalyst-Heating Operation in a Medium-Duty Diesel Engine: Operating Strategy Calibration, Fuel Reactivity, and Fuel Oxygen Effects." SAE Technical Paper 2021, DOI: https://doi.org/10.4271/2021-01-1182.
2. Sharp, C., Henry, C., Yoon, S., Carter, M. et al. "Achieving Ultra Low NOX Emissions Levels with a 2017 Heavy-Duty On-Highway TC Diesel Engine - Comparison of Advanced Technology Approaches." *SAE Int. J. Engines* 10(4):1722-35, 2017, https://doi.org/10.4271/2017-01-0956.
3. Kurtz, E. and Polonowski, C. J., "The Influence of Fuel Cetane Number on Catalyst Light-Off Operation in a Modern Diesel Engine." SAE Int. J. Fuels Lubr. 10(3), 2017, DOI: https://doi.org/10.4271/2017-01-9378.
4. Somhorst, J., Bovo, M., Oevermann, M., and Denbratt, I., "A Method to Evaluate the Compression Ratio in IC Engines with Porous Thermal Barrier Coatings." SAE Technical Paper 2018, DOI: https://doi.org/10.4271/2018-01-1778.
5. U.S. Department of Energy, "Co-optimization of Fuels & Engines." accessed June 24, 2021, Available online: https://www.energy.gov/eere/bioenergy/co-optimization-fuels-engines. .
6. Woschni, G., "A Universally Applicable Equation for the Instantaneous Heat Transfer Coefficient in the Internal Combustion Engine." SAE Technical Paper 670931, 1967, DOI: https://doi.org/10.4271/670931.
7. Koci, C. P., Fitzgerald, R. P., Ikonomou, V., and Sun, K., "The effects of fuel–air mixing and injector dribble on diesel unburned hydrocarbon emissions." 20(1):105-27, 2019, 10.1177/1468087418821827.
8. Musculus, M. P. B., Miles, P. C., and Pickett, L. M., "Conceptual models for partially premixed low-temperature diesel combustion." *Progress in Energy and Combustion Science* 39(2):246-83, 2013/04/01/ 2013, https://doi.org/10.1016/j.pecs.2012.09.001.
9. Graham, L., "Chemical characterization of emissions from advanced technology light-duty vehicles." *Atmospheric Environment* 39(13):2385-98, 2005/04/01/ 2005, https://doi.org/10.1016/j.atmosenv.2004.10.049.
10. "Musculus and Kattke Model." https://ecn.sandia.gov/download-code/.
11. Musculus, M. P. B. and Kattke, K., "Entrainment Waves in Diesel Jets." *SAE Int. J. Engines* 2(1):1170-93, 2009, https://doi.org/10.4271/2009-01-1355.
12. Abramovich, G. N. *Chapter 5: Jet of an Incompressible Fluid in a Coflowing External Stream, The Theory of Turbulent Jets.* Cambridge, MA, USA: The MIT Press, 1963.
13. Genzale, C. L., Idicheria, C. A., Manin, J., Pickett, L. M. et al, "Relationship Between Diesel Fuel Spray Vapor Penetration/Dispersion and Local Fuel Mixture Fraction." SAE Int. J. Engines 4(1): 764-99, 2011, DOI: https://doi.org/10.4271/2011-01-0686.
14. Payri, R., Bardi, M., Gimeno, J., Pickett, L. M. et al, "Transient Rate of Injection Effects on Spray Development." SAE Technical Paper 2013, DOI: https://doi.org/10.4271/2013-24-0001.
15. Burcat, A. R., B. *Third millenium ideal gas and condensed phase thermochemical database for combustion (with update from active thermochemical tables)*, USDOE Office of Science, 2005, https://doi.org/10.2172/925269.
16. Heywood, J. B. *Internal combustion engine fundamentals.* McGraw-Hill Education, 2018.
17. Goodwin, D. G., Speth, R. L., Moffat, H. K., and Weber, B. W., "An object-oriented software toolkit for chemical kinetics, thermodynamics, and transport processes." https://www.cantera.org.

10/19/2016

18. Busch, S., "Diesel-like fuels, combustion, and emissions." presented at 2021 DOE Vehicle Technologies Office Annual Merit Review, accessed June 24, 2021, Available online: https://www.energy.gov/eere/vehicles/articles/diesel-fuels-combustion-and-emissions. .

19. Skeen, S., Manin, J., and Pickett, L. M. J. S. I. J. o. E., "Visualization of Ignition Processes in High-Pressure Sprays with Multiple Injections of n-Dodecane." *SAE Int. J. Engines* 8(2):696-715, 2015, https://doi.org/10.4271/2015-01-0799.

20. Westbrook, C. K., "Chemical kinetics of hydrocarbon ignition in practical combustion systems." *Proceedings of the Combustion Institute* 28(2):1563-77, 2000/01/01/ 2000, https://doi.org/10.1016/S0082-0784(00)80554-8.

21. Dahms, R. N., Paczko, G. A., Skeen, S. A., and Pickett, L. M., "Understanding the ignition mechanism of high-pressure spray flames." *Proceedings of the Combustion Institute* 36(2):2615-23, 2017/01/01/ 2017, https://doi.org/10.1016/j.proci.2016.08.023.

Contact Information

Seokwon Cho
scho@sandia.gov

Acknowledgements

Definitions/Abbreviations

aTDC	After top-dead center
bTDC	Before top-dead center
CA	Crank angle
CN	Cetane number
CO	Carbon monoxide
CO$_2$	Carbon dioxide
DOE	Duration of energizing
EGR	Exhaust gas recirculation
EVO	Exhaust valve opening
H/C	Hydrogen-to-carbon ratio
H$_2$CO	Formaldehyde
HoV	Heat of vaporization
HTHR	High-temperature heat-release
IBP	Initial boiling point
IMEP, IMEP$_n$	Indicated mean effective pressure, net indicated mean effective pressure
LTHR	Low-temperature heat-release
MFB10	10% mass fraction burn point
N$_2$	Molecular nitrogen
O$_2$	Molecular oxygen
O/C	Oxygen-to-carbon ratio
ROI	Rate of injection
SCR	Selective catalytic reduction
SOE	Start of energizing
TDC	Top-dead center

10/19/2016

Symbol	Definition
UHC	Unburned hydrocarbons
Q_{total}	Total amount of heat-release
Q_{LHV}	Lower heating value of fuel
A_{cyl}	Instantaneous combustion chamber surface area
B	Bore diameter
C_1	Motored velocity scale factor in Woschni heat transfer correlation
C_2	Combustion-induced velocity scaling factor in Woschni heat transfer correlation
C_m	Woschni tuning parameter
$c_{p,exhaust}$	Constant pressure heat capacity of exhaust gas
C_v	Constant volume heat capacity
ΔT	Temperature difference between exhaust gas and ambient
γ	Ratio of specific heats
h	Specific enthalpy
h_f	Enthalpy of fuel
h_{gas}	Enthalpy of ambient gas
$h_{Woschni}$	Convective heat transfer coefficient according to Woschni's correlation
m	Mixture mass
$\dot{m}_{air}$	Air mass flow rate
m_{fuel}	Mass of fuel per cycle
$\dot{m}_{fuel}$	Fuel mass flow rate
n	Engine speed
η_{comb}	Combustion efficiency
P	Fired cylinder pressure
P_r	Referenced cylinder pressure
Φ_{ex}	Exhaust heat flux
$Q_{incomplete\ combustion}$	Incomplete combustion loss
Q_{wall}	Wall heat-loss (cumulative)
R	Gas constant
$\bar{R}$	Universal gas constant
S_{mp}	Mean piston speed
T	Mixture temperature
T_{cyl}	Bulk gas temperature
T_f	Fuel temperature
T_r	Referenced cylinder temperature
T_{wall}	Wall temperature
t	Time
θ	Crank angle
V	Mixture volume
V_d	Engine displacement volume
V_r	Referenced cylinder volume
$\dot{w}$	Net production rate